Atmospheric
Chemistry
and Physics
Discussions

EGU

Ice-nucleating particles impact the severity of precipitations in West Texas

Hemanth S. K. Vepuri[1,*], Cheyanne A. Rodriguez[1], Dimitri G. Georgakopoulos[4], Dustin Hume[2], James Webb[2], Greg D. Mayer[3], and Naruki Hiranuma[1,*]

[1]Department of Life, Earth and Environmental Sciences, West Texas A&M University, Canyon, TX, USA
[2]Office of Information Technology, West Texas A&M University, Canyon, TX, USA
[3]Department of Environmental Toxicology, Texas Tech University, Lubbock, TX, USA
[4]Department of Crop Science, Agricultural University of Athens, Athens, Greece

*Corresponding authors: hsvepuri1@buffs.wtamu.edu and nhiranuma@wtamu.edu

Abstract

Ice-nucleating particles (INPs) influence the formation of ice crystals in clouds and many types of precipitation. However, our knowledge of the relationship between INPs and precipitation is still insufficient. This study was conducted to fill this gap by assessing precipitation properties and INP concentrations (n_{INP}) from a total of 42 precipitation events observed in the Texas Panhandle region from June 2018 to July 2019. We used a cold-stage instrument called the West Texas Cryogenic Refrigerator Applied to Freezing Test system to estimate n_{INP} through immersion freezing in our precipitation samples. A disdrometer was used to measure the precipitation intensity and size of precipitating particles during each precipitation event. The analysis of yearlong precipitation properties as well as INPs for the samples shed a light on the seasonal variation of the n_{INP} values in West Texas. Furthermore, we characterized the bacteria speciation of the storm and ambient dust samples collected at a commercial feedlot in West Texas to identify potential biological sources of INPs in our precipitation samples. Overall, our results showed a positive correlation between n_{INP} and intensity of precipitation with notably large hydrometeor sizes in storm precipitations. Amongst all observed precipitation types, the highest INPs were found in the snow samples, and hail/thunderstorm samples have the highest INPs at high temperature -5°C.

1 Introduction

1.1. What are INPs?

Aerosol particles play a major role in altering the cloud properties, precipitation patterns, and ultimately the Earth's radiation budget (Lohmann and Feichter, 2005). In the past few decades, the aerosol particle direct effects (i.e., the impact of aerosol particles on net radiation through scattering and absorption of solar radiation) have been extensively studied (Satheesh and Krishna Moorthy, 2005). For example, the global radiative forcing by sea salt aerosols and dust is known to be in the range of −0.5 to −2 W m^{-2} and −2 to +0.5 W m^{-2}, respectively.

Atmospheric
Chemistry
and Physics
Discussions

Open Access

EGU

35 However, the aerosol particle indirect effects (i.e., radiative impact due to formation of clouds) have been enigmatic. Some atmospheric aerosol particles are known to act as ice-nucleating particles (INPs) and catalyze the formation of ice crystals in the clouds, but their overall impact on the Earth's radiative budget remains quantitatively uncertain (Lohmann et al., 2007).

40 While INPs are sparse in the atmosphere, they have substantial impacts on the cloud microphysics and the precipitation formation (DeMott et al., 2010). The sources of atmospheric INPs are diverse as they emerge naturally and also through human activities, adding complexities to our comprehensive understanding in their impacts (e.g., Kanji et al., 2017; Zhao et al., 2019). In general, INPs provide a surface on which the water vapor and/or cloud droplet deposits and freezes (Van den Heever et al., 2006). This type of ice formation in the
45 presence of INP is known as heterogenous freezing (Vali et al., 2015). In the absence of INPs, the formation of atmospheric ice particles follows the process of homogeneous nucleation, in which it requires the cloud droplet to be supercooled to the temperature (T) of -32°C and below (depending on the pure water droplet size) to form ice crystals (Koop et al., 2000; Koop and Murray, 2016). Though our knowledge regarding INP remains insufficient, there have been advances in understanding the different modes of heterogeneous ice nucleation
50 (IN) in the atmosphere in the last few decades. For example, deposition nucleation is induced by the direct deposition of water vapor on to an INP's surface and ice embryo formation on the surface under ice supersaturation conditions (Kanji and Abbatt, 2006; Möhler et al., 2008). Recently, some studies have argued that the deposition nucleation could be interpreted as pore condensation and freezing (Marcolli, 2014). The presence of water in pores of mineral materials and the resulting inverse Kelvin effect cause an instantaneous
55 water saturation condition in the confined space, allowing the water to freeze even at water sub-saturated ambient conditions (David et al., 2019; Marcolli, 2014). Amongst various IN paths, perhaps the most important mode is immersion freezing (De Boer et al., 2010). This process starts with the formation of cloud droplet followed by freezing due to an INP immersed in the supercooled droplet. In addition, the past studies have identified other modes of heterogeneous nucleation, such as condensation freezing (Belosi and Santachiara,
60 2019), contact freezing (Hoffmann et al., 2013) and inside-out evaporation freezing (Durant and Shaw, 2005). These modes are relatively less relevant in the mixed-phase clouds (MPCs) as discussed in the next section.

1.2. Importance of Immersion Freezing

65 INPs greatly influence cloud properties, especially in MPCs, which are typically observed in the altitude range of 2 km to 9 km above ground level (Hartmann et al., 1992). Out of all heterogeneous ice-nucleation modes, the immersion freezing is the most dominant mode of ice formation in MPCs (Ansmann et al., 2008; De Boer et al., 2010; Hande and Hoose, 2017; Vergara-Temprado et al., 2018). In Hande and Hoose (2017), different cloud types such as orographic, stratiform and deep-convective systems were simulated and analyzed for different
70 freezing modes under various polluted conditions. The authors demonstrate that immersion freezing is the predominant IN mode under various simulated circumstances, accounting for 85 to 99%, while other IN paths play a less significant role. Cui et al. (2006) also showed that immersion freezing is the primary mode of ice formation with little significance of the deposition mode in the early stages of the cloud development. Moreover, whereas contact freezing may be a highly efficient ice formation path, a previous simulation study showed that
75 it is a negligible mode in the given MPC conditions (Phillips et al., 2007). Field et al. (2012) and De Boer et al.

Atmospheric
Chemistry
and Physics
Discussions
Open Access
EGU

(2011) showed that the formation of cloud droplets is a precondition for ice formation in MPCs, thus highlighting the importance of immersion nucleation. Furthermore, using multiple ground-based instruments, including Lidar, AERONET Sun Photometer, and Vaisala Radiosonde, Ansmann et al. (2008) found that a high INP concentration (n_{INP}) (i.e., ~ $1 - 20$ cm^{-3}) in the Saharan dust. This high dust-including n_{INP} episode coincided with the presence of liquid droplets at cloud tops at Ts of -22°C to -25°C. Similarly, Ansmann et al. (2009) shows the observation of tropical altocumulus clouds having the liquid cloud tops. Due to the importance and dominance of immersion freezing, the current study focuses on measuring the immersion freezing efficiency of the precipitation samples collected in the Texas Panhandle region.

1.3. INPs and Atmospheric Precipitation

It is known that INPs in MPCs have a notable impact on the properties of precipitation. Previously, Yang et al. (2019) studied the effect of INPs on cloud dynamics and precipitation through model simulations of an observed severe storm in Northern China. The authors show that an increase in INPs can enhance the storm, whereas an excessive increase of INPs may impede the updrafts in the storm. The reason for this complex effect of INPs may be explained by the variation in the latent heat release in the convective system at different stages of its development. This latent heat is further influenced by INP episode, thus affecting the dynamics of the precipitation system. Furthermore, the increase in INP number might reduce the mean hail diameter (hail particles with smaller diameters melt more easily), which leads to decreased hail precipitation and an increased rain formation in contrast to the previous studies (Fan et al., 2017; Van den Heever et al., 2006). Similar results have been found by Chen et al. (2019). The authors show that an increased n_{INP} in the simulated hailstorm can reduce the graupel size and reduce the concentration of hail stones. Likewise, the aircraft observations along with the model simulations of convective storms in West Texas and U.S. High Plains have shown that the addition of INPs at the base of warm clouds would result in an increase of the precipitation amount by strong updrafts in the system (Rosenfeld et al., 2008), ultimately affecting the local hydrological cycle (Mülmenstädt et al., 2015). It has also been observed that INPs can be removed from the atmosphere through precipitation resulting in a net decrease in n_{INP}, affecting the precipitation development (Stopelli et al., 2015). The estimation of n_{INP} in this study from the precipitation samples gives a quantitative approximation of INPs in the locally observed weather systems, potentially allowing us to parameterize the INP-precipitation relationship.

Several previous studies have characterized the n_{INP} in the precipitation samples from various locations (Creamean et al., 2019; Petters and Wright, 2015; Levin et al., 2019). Petters and Wright (2015) reported a wide range of n_{INP} values in their local precipitation samples collected approximately 3 km west of Raleigh, NC, USA for July 2012 and October 2013. Their study shows a variation of 10 orders of magnitude in the concentrations of INPs with a high variability in the T range of -5°C to -12°C, suggesting inclusion of biological INPs, which are generally known to be active at relatively high freezing Ts (Després et al., 2012). The lower limit for the INP spectrum as a function of T derived from the cloud water and precipitation samples in Petters and Wright (2015) may highlight the extreme rarity of INPs at Ts warmer than -10°C. Particularly, the authors showed that the highest ever observed n_{INP} at -8°C were three orders of magnitude lower than observed ice crystal concentrations in tropical cumuli at the same temperature. More precipitation studies may provide a constraint on minimum enhancement factors for secondary ice formation processes. In Levin et al. (2019) the n_{INP} values

115   during an atmospheric river event on the west coast of United States were studied. The authors found an
increased concentration of marine INPs in contrast to their previous studies, showing high mineral/soil dust
during an atmospheric river precipitation. However, the relation between INPs and the physical properties of
precipitation particles as well as the variation in severity of the precipitation is still uncertain, representing a
knowledge gap regarding precipitation INPs. This study narrows this gap by investigating the role of INPs in
120   different precipitation systems.

1.4. Study Objectives

In this study, we calculated the n_{INP} in precipitation samples collected in the Texas Panhandle region.
All of our samples were analyzed at our laboratory using a cold stage instrument. The estimated n_{INP} in the
precipitation samples were compared with precipitation properties, such as the intensity of precipitation (mm
125   hr^{-1}) and hydrometeor particle size (mm). In addition, the seasonal variation of n_{INP} in the Texas Panhandle
region was studied and compared with the particulate matter (PM) concentrations measured by our Internet
of Things (IoT) sensors. A subset of the collected precipitation samples was analyzed for their bio-speciation to
characterize potential biological INP sources in the West Texas region and also to investigate if the biological
composition matches with any previously known high T biological INPs.

130   ## 2 Methods

2.1 Precipitation Sampling

In this study, the precipitation samples were collected from different seasons throughout the year
during June 2018 – July 2019. Sterilized Polypropylene tubes of 50 ml (VWR® Centrifuge Tube) were used as
sampling gauges. The gauges were placed at ~50 ft above the ground on the rooftop of Natural Science Building
135   at West Texas A&M University, Canyon, TX. This particular location was chosen to avoid any obstruction for
our sampling activities. The sampling tubes were well exposed to the ambient air without any canopies
throughout the sampling process. The sampling gauges were replaced every 24 hours to minimize the effect of
dry deposition prior to the precipitation sample collection. A blank dry deposition sample (Sample# 34) was
specifically collected for 24 hours from January 2-3, 2019 in order to examine and quantify the effect of dry
140   deposition on n_{INP}. The freezing spectrum of this dry deposition sample (suspended in HPLC grade pure water)
was later compared with the IN spectra of precipitation samples (see Sect. 3.3.1). For the duration of a given
precipitation episode, some amount of sample was accumulated in the tube. The sampling tubes were then
capped and stored at T of 4°C in the refrigerator, following the method described in Petters and Wright (2015),
until the droplet-freezing assay experiments were commenced. The effect of storage conditions on the IN
145   activity was not considered in this study. We note that Beall et al. (2020) recently found a decrease in
precipitation n_{INP} by 42% when stored at 4°C and suggested correction factors for the T range of -7°C to -17°C.
After the freezing experiment, a subset of our samples was kept under deep-freezing conditions (-80°C) for
further biological analysis (see Sect. 2.6). In total, 42 precipitation samples were collected from different
weather systems. In this study we estimated the n_{INP} values from (1) snows, (2) hails/thunderstorms, (3) long-

Atmospheric
Chemistry
and Physics
Discussions

150 lasted rains, and (4) weak rains. More information about the samples used in this study, precipitation types and the amount of the precipitation collected for each sample are provided in the Supplemental Information (SI) Table S1-1.

2.2. Disdrometer Measurements of Precipitation Properties

For our precipitation measurements, we used the OTT Parsivel^2 (Particle Size Velocity 2) sensor. This
155 device is a modern laser-optical disdrometer (λ = 780 nm) which measures the size and fall velocity of precipitating particles. The OTT Parsivel^2 was deployed in side-by-side position with the precipitation gauge collector for the duration of our study period. A detailed technical description of OTT Parsivel^2 is given in a previous study (Tokay et al., 2014), so only a brief description is provided here. A combination of the laser transmitter and receiver component was integrated as a single cluster in a weatherproof housing and detect
160 precipitation particles passing through a horizontal strip of light. A nominal cross section area of a laser beam detection was 54 cm^2, and the system recorded the number of hydrometeors in a 32 x 32 matrix (i.e., fall velocity x diameter) in the $\geq$ 30 seconds time resolution. The measurable size range of hydrometeor particles was 0.062 - 24.5 mm in diameter (D_p) with bin size intervals (ΔD_p) varying from 0.125 to 3.0 mm. Our disdrometer was coupled with an OTT netDL Hydrosystem logger (40 channels). The OTT Parsivel^2 also
165 measured the intensity of precipitation (mm hr^{-1}) and the number of precipitation particles passing through the horizontal strip of light in the event of precipitation. The OTT Parsivel^2 automatically categorized the precipitation type according to the National Weather Service (NWS) weather code based on the measured precipitation properties. Due to the intermittent nature of the precipitation, the OTT Parsivel^2 assigned multiple NWS precipitation codes during a single precipitation event (Table S1-1 column 'NWS Code'). We compared
170 our manual observations with the NWS precipitation code assigned by the disdrometer, and we categorized all observed precipitations into four different types. These four major precipitation types defined in this study included snow, hail/thunderstorm, long-lasted rain, and weak rain. More detailed methodology of precipitation categorization is discussed in SI S1.1.

2.3 IoT Air Quality Sensor Measurements

175 A cluster of Arduino-based IoT air quality sensors was developed to measure ambient air conditions at our precipitation sampling location. This IoT cluster was deployed alongside the disdrometer and sampling gauge to complement this study. A DFRobot PM laser dust sensor measured PM with size ranges of < 1 μm (PM$_{1.0}$), < 2.5 μm (PM$_{2.5}$), and < 10 μm (PM$_{10}$). Other ambient conditions, including T, barometric pressure, and humidity, were measured with a precision Bosch BME280 environmental sensor. We calibrated our sensors
180 against a commercially available sensor (GlobalSat Inc., LS-113). Our sensors utilized Long Range and Wide Area Network (LoRaWAN) technology for data transmission. A LoRaWAN transceiver is connected to our sensors for wireless data transmission. This small IoT device operated with 915 MHz signal frequency, transmitting encrypted and signed packets of captured air quality data through a hosted LoRa network server to a Kibana visualization server. This data interface enabled in situ monitoring and processing of the data. The PM concentrations were
185 later time-averaged for comparison with the precipitation properties and n_{INP} in the precipitation samples.

2.4 Immersion Freezing Experiment

All immersion freezing experiments in this study were conducted using an offline instrument called West Texas - Cryogenic Refrigerator Applied to Freezing Test (WT-CRAFT) system (Hiranuma et al., 2019; Cory et al., 2019; Rodriguez et al., 2020). The WT-CRAFT system is a cold-stage technique in which the droplets are placed on an aluminum plate and cooled until they are frozen. A commercially available digital camera was used to record the droplet freezing events, and we visually evaluated the freezing Ts based on the shift in droplet brightness while freezing. If there was an uncertainty in determining the T at which a droplet was completely frozen, we used the ImageJ software for further image analysis of those droplets (see Table S4 in Hiranuma et al., 2019). This system was used to obtain T-resolved n_{INP} in -25°C < T < 0°C. The lower T limit was -25°C to ensure measuring INPs with negligible artefacts (Hiranuma et al., 2019). Our system is susceptible to low INP detection, and the minimum INP detection limit of the WT-CRAFT system for this study was 0.002 L^{-1} air. To minimize any contamination during the IN measurement, the WT-CRAFT system was placed in a ventilated fume hood. For each experiment an aluminum plate surface was freshly coated with a thin layer of thermally conductive and IN-inert Vaseline to physically isolate individual droplets from the aluminum surface (otherwise, aluminum can act as a heterogeneous IN surface). A total of 70 suspension droplets of 3µL volume each were prepared for each run. The aluminum plate with the droplets on it was then placed inside a portable cryogenic refrigerator (Cryo-Porter). Freezing Ts were measured by the sensor taped on the aluminum surface with a resolution of 0.1°C, and the external keypad controller was used to control cooling rate (°C min^{-1}). In this study, the freezing experiments were carried out at a cooling rate of 1°C min^{-1}. The validity of using this cooling rate and another test regarding time trial aspect are demonstrated in SI S2 (Figs. S2-1 and S2-2). The droplets were cooled until all 70 droplets were frozen before warming up the system to 5°C to be prepared for a subsequent experiment.

If all the droplets were frozen at T > -25°C, a HPLC-grade ultrapure water was used to prepare different serial dilutions for the precipitation samples. The diluted suspensions were made to compute the n_{INP} down to -25°C. Some of our precipitation samples were diluted until the frozen fraction (the ratio of number of droplets frozen to the total number of droplets) curve was conformed to the background curve (i.e., frozen fraction curve for the HPLC ultrapure water). At the end each WT-CRAFT experiment, the frozen fraction and ambient n_{INP} were estimated as a function of T with an interval of 0.5°C. The IN measurements from the undiluted and diluted runs were merged by taking the lower n_{INP} values for the overlapped T region.

The total systematic T uncertainty in our experiments for this study was ± 0.5°C (Hiranuma et al., 2019). The uncertainty in our estimated n_{INP} were estimated using the 95% confidence interval method described in Schiebel (2017). Background contamination tests for WT-CRAFT were carried out weekly to make sure negligible background freezing at -25°C. In this study, we consider the frozen fraction ≤ 0.05, accounting for less than 3% of pure water activation, as negligible background (Hiranuma et al., 2019). For these background tests, only HPLC grade ultrapure water was used for preparing the droplets.

2.5 IN Parameterization

Here we describe the parameterization used to estimate ambient n_{INP}. Initially, we computed the $C_{INP}(T)$

225 value, which is the nucleus concentration in precipitation suspension (L^{-1} water) at a given T as described in Vali (1971). This $C_{INP}(T)$ value was calculated as a function of unfrozen fraction, $f_{unfrozen}(T)$ (i.e., the ratio of number of droplets unfrozen to the total number of droplets) as:

230

$$C_{INP}(T) = - \frac{\ln \left(f_{unfrozen}(T) \right)}{V_d} \tag{1}$$

in which, V_d is the volume of the droplet (3 μL).

Next, we used the cloud water content (CWC) parameter in order to convert $C_{INP}(T)$ to $n_{INP}(T)$, INP in
235 the unit volume of atmospheric air at standard T and pressure (STP) conditions, which is 273.15 K and 1013 mbar. We presumed CWC to be a constant of 0.4 g m^{-3}, covering the continental clouds in our study. Our assumption would be reasonable since Petters and Wright (2015) showed that the variation of n_{INP} with CWC values for different cloud types in the atmosphere would typically be limited within a factor of two, and our n_{INP} uncertainties could be larger than that. Thus, the effect of CWC on the n_{INP} would be negligible.

240 The sample air volume (V_{air}) at the cloud level was calculated by converting the volume of the precipitation sample collected (V_l) using the Eqn. (2) from Petters and Wright, 2015:

$$V_{air} = \frac{V_l \times 1000 \times \rho_w}{CWC}$$

$$\tag{2}$$

245 where ρ_w is a unit density of water (1 g ml^{-1}). V_{air} is in liters (L), whereas V_l is given in ml. The multiplication factor '1000' is used to convert the volume from cubic meter (m^3) of air to liter of air. The cumulative n_{INP} per unit volume of sample air, described in the previous study DeMott et al. (2017), was then estimated as:

$$n_{INP}(T) = C_{INP}(T) \times (DF) \times \frac{V_l}{V_{air}} \tag{3}$$

where DF is a serial dilution factor (e.g., DF = 1 or 10 or 100 and so on).

250

2.6. Microbiome of feedlot dust and precipitation samples

The overall goal of our metagenomics analysis was to identify known ice-nucleation-active bacterial and fungal species in feedlot dust and precipitation samples collected in the West Texas region. In this study, we have examined a heterogenous set of samples including feedlot samples, hail, long-lasted rain and a 24-hour dry deposition sample. Next, we describe our microbiome analysis procedure in four different steps, including (1) DNA Extraction, (2) 16S rRNA Amplicon Diversity Sequencing, (3) Bioinformatics, and (4) Data Analysis. For DNA extraction, Genomic DNA was first extracted from all samples using PowerSoil DNA Isolation Kits (MoBio Laboratories, Inc., Carlsbad, CA, USA). Extraction proceeded following the manufacturer's protocol, with the following minor changes: solutions C1 and C6 were heated to 65°C and solution C6 was allowed to remain on the filter membrane for at least one minute before centrifugation. Additionally, the C6 step was repeated. Library preparation for bacterial 16S DNA amplicon sequencing utilized primers for the V1-V3 hypervariable region of the 16S gene. These primers were constructed for the 16S amplicon using a combination of the 28F and Illumina i5 sequencing primer and the Illumina i7 sequencing primer with the 519R primer. Amplifications were performed in 25 μl reactions with Qiagen HotStar Taq master mix (Qiagen Inc, Valencia, CA, USA). Reactions were performed with 1 μl of each 5μM primer and the template DNA. Amplification was performed on an ABI Veriti thermocycler (Applied Biosytems, Carlsbad, CA, USA) under the following thermal profile: 95°C for 5 min, then 25 cycles of 94°C for 30 sec, 54°C for 40 sec, 72°C for 1 min, followed by one cycle of 72°C for 10 min and 4°C hold. An ethidium bromide stained gel was used to qualitatively determine the amount of the amplification product to add to the second amplification stage. Primers for the second PCR were designed based on the Illumina Nextera PCR primers. The second stage amplification proceeded using the same cycling protocol as the first round, except it was amplified for only 10 cycles. SPRIselect beads (BeckmanCoulter, Indianapolis, IN, USA) were used at a 0.7 ratio to size-select the DNA amplicons from an equimolar pooled sample. Pooled samples were then quantified using a Quibit 2.0 fluorometer (Life Technologies) and loaded on an Illumina MiSeq (Illumina, Inc. San Diego, CA, USA) 2x300 flow cell at 10pM.

For bioinformatics, raw data were initially processed using a standard microbial diversity analysis pipeline (QIIME2-2020). Raw data was first checked for sequencing quality and chimeric sequences, before being parsed through a microbial diversity pipeline. During the cleanup stage; denoising of the raw data was performed using various techniques to remove short sequences, singleton sequences, and reads with poor quality scores. Next, chimera detection software was used to filter out any potentially chimeric sequences. Finally, remaining high-quality sequences were corrected base by base to check for sequencer miscalls. The diversity analysis pipeline clustered all sequences based on 97% similarity to yield operational taxonomic units (OTUs), before running a seed sequence from each OTU through a taxonomic database curated in-house by RTLGenomics. Finally, the taxonomy was assigned to each sequence using a classifier that was pretrained on GreenGenes database with 99% OTUs. The relative abundance of bacterial taxa within each sediment sample was determined by dividing each OTU by the total number of reads. Alpha diversity was carried out by taking phylogenetic distances into account and by looking at how diverse the phylogentic tree is for each sample. Next, beta diversities were analyzed using weighted (by bacterial abundance) or unweighted Unifrac distances calculated from a mid-point rooted tree. Multivariate differences in beta diversity were analyzed using Permutational Multivariate Analysis of Variance Using Distance Matrices function (ADONIS), which uses an ANOVA-like simulation to test for sampling location differences (McMurdie and Holmes 2013).

3 Results and Discussion

3.1 Ambient and Precipitation Properties

The time series summary of ambient and precipitation properties measured by our disdrometer as well as IoT cluster, respectively, is shown in Fig. 1. All the individual T and relative humidity data points shown in Fig. 1a and 1b correspond to the sampling start date of each precipitation event. A notable seasonal variation of atmospheric T was observed. Each data point in Fig. 1a show the average temperature measured over the sampling period of a given precipitation event. The highest average temperature measured during a precipitation event was 34.9°C ± 12.2, which was in the summer of 2018 (i.e., 16 July; ID# 7; a long-lasted rain sample), while the lowest T was -6.5°C ± 6.7, measured during the winter of 2018 (i.e., 28 Dec; ID# 23; a snow sample). The annual mean T for Canyon, TX region measured at our sampling site was 17.7°C. The details of each precipitation event and its properties are shown in the SI Table S1-1 and S1-2. The diurnal cycles of ambient properties are not shown in Fig. 1a. Nevertheless, we typically observed suppression of T before precipitation events in our study. It has been understood that the T gradient plays a major role in the development and growth of the precipitation systems (Vaid and Liang 2015). The relative humidity shown in Fig. 1b was the averaged value for each precipitation sampling period. The highest and lowest relative humidity values measured were 70.7% ± 2.3 (on 12 March 2019; ID# 26; a weak rain sample) and 30.8% ± 0.7 (on 16 July 2018; ID# 7; a long-lasted rain sample). Figure 1c displays the time series of the cumulative number of detected precipitation particles in individual precipitation events and the overall mean number of detected particles (dashed line). In our study period, the precipitation events during September 2018 – January 2019 exhibited a substantial number of precipitation particles with a cumulative number of 2E+05 to 6.6E+05 per event. This high number of precipitation particles, greater than the overall mean cumulative number (i.e., 7.9E+04) was observed in conjunction with snow/hail-involving precipitation events during this period. Out of all the 42 samples, the highest number of precipitation particles detected were 6.6E+05 (on 5 Nov, 2018; ID# 19; a snow sample), while the lowest was 1.0E+04 (2 Sep, 2018; ID# 13; weak rain). Additional information is detailed in SI Table S1-2 and S1-3. There were other occasional snow/hail precipitation events in our study period, but the frequency of their occurrence was indeed high in Fall - Winter. Overall, a high average number of precipitation particles were detected for all the snow samples combined, 2E+05 ± 2E+02, followed by hail/thunderstorm samples, 7.1E+04 ± 1.9E+04. On the other hand, the weak rain episode had lowest average number of precipitation particles, 1.8E+04 ± 5.4E+03 (SI Table S1-3). Figure 1d shows the average, maximum and minimum precipitation intensity (mm hr^{-1}) measured during each precipitation event. Due to the intermittent nature of the precipitation, the intensity widely ranged from 0 to 150 mm hr^{-1} per event. The measured lower values of the average intensity were due to the influence of low intensities observed over a prolonged period of a given precipitation event. The highest maximum intensity of 129.3 mm hr^{-1} was measured during a hail/thunderstorm event (ID# 40), while the lowest was 1.1 mm hr^{-1} during a snow event (ID# 23). The average intensity ± standard error for each precipitation category is shown in the SI Table S1-3. Hail/thunderstorm events have recorded the highest average precipitation intensity of 5.3 ± 7E-01 mm hr^{-1}, which was greater than the average intensity measured for the weak rain episodes, 1.5 ± 3.8E-01 mm hr^{-1} by a factor of 3 (SI Table S1-3).

The variation of precipitation properties was further investigated by analyzing the size distribution of precipitation particles. Figure 2 shows the log-normal particle diameter distribution for each category of
335 precipitation system. These size distributions were computed from the size-resolved precipitation particle measurements by the OTT Parsivel[2] disdrometer during each precipitation event. The size of precipitation particles was represented at the mid-value of the corresponding size bin. As shown in the Fig. 2a and 2b, both the snow and hail/thunderstorm samples had particles of diameter greater than 10 mm, and the maximum particle diameter was 17 mm. Although there are three episodes of long-lasted rain with a particle diameter
340 greater than 14 mm (Fig. 2c), a clear trend of overall decrease in the hydrometeor size was seen for this category as well as the weak rain samples (Fig. 2d). Even though the number of samples in each precipitation category was different, 66.7% (4 samples) of the total snow samples (n=6) had precipitation particles of diameter ≥ 8.5 mm. Less compared to snow, but 55.6% (10 samples) and 46% (6 samples) of the hail/thunderstorms (n=18) and long-lasted rain (n=13) samples, respectively, had recorded precipitation particles of diameter ≥ 8.5 mm.
345 In contrast, none of the weak rain samples (n=5) had hydrometeors of diameter ≥ 8.5 mm, and all weak rain samples contained particles only smaller than 6.5 mm. Moreover, the mode precipitation particle diameter for the snow, hail/thunderstorm, and long-lasted rain samples was 0.44 mm, whereas it was 0.31 mm for the weak rain samples (see SI Table S1-3). This variation in mode diameter along with the results shown in Fig. 2 exhibited the shift in hydrometeor particle size distribution towards a higher diameter with an increased intensity of
350 precipitation. Further discussion regarding the variation of n_{INP} with the severity of precipitation was analyzed and is followed in Section 3.3.

3.2 IoT Air Quality Sensor Results

An IoT air quality sensor-measured PM concentrations were also analyzed for each precipitation
355 sampling period to understand the effect of wet deposition of PMs on INPs. Figure 3 shows the time series of average PM concentrations observed during each precipitation episode, overall mean PM values, and the hourly PM data. The overall mean ± standard error PM concentrations calculated from over one year of data were 3.9E+00 ± 9.2E-02 (PM$_{1.0}$), 4E+00 ± 4.5E-02 (PM$_{2.5}$), and 1E+01 ± 2.2E-01 (PM$_{10}$) μg m^{-3}. Although, there was an inconsistent variation of PM concentrations with precipitation type, we observed a substantial increase
360 in all PM values for the period July – Aug 2018 and May 2019. In contrast, a decrease in all PM concentrations was observed during Sep 2018 – Mar 2019. This increase in PM values during summer and decrease during winter suggested the seasonal variation at the sampling site. In addition, the influence of PM values on n_{INP} from each precipitation event was analyzed at -10°C, -15°C, -20°C, and -25°C. The Pearson correlation coefficients (R-value) at -10°C, -15°C, -20°C, and -25°C were statistically insignificant and negative for all PM
365 types (SI Fig. S3). These results suggested no strong positive correlation between the PM and n_{INP} for our sampling period. Moreover, we did not observe a clear sign of wet deposition during a given precipitation event (Stopelli et al., 2015), as there was no decrease in the original hourly PM concentrations during or after the precipitation. Overall, our PM analysis had suggested a local seasonal variation in PM concentrations, and no significant relation between PM and n_{INP} values from our precipitation samples.

3.3 INP Results

3.3.1 $n_{INP}(T)$ spectra of each precipitation type

Figure 4 shows the IN spectra for different precipitation types analyzed in this study superposed on the IN spectral boundaries adapted from a previous precipitation INP study (Petters and Wright, 2015). This figure also displays other reference IN spectra, including our 24-hour dry deposition blank sample (collected from January 2 – 3, 2019 at our sampling site) and IN spectra measured for dust suspension samples collected from the downwind side of a local feedlot (identity purposely concealed), where substantial and consistent dust emission historically persists (Whiteside et al., 2018). For the measured T range, n_{INP} values from dry deposition blank sample were at least an order of magnitude lower than that from our precipitation samples. This finding corroborated our assumption of negligible contribution of dry deposition in our WT-CRAFT estimated n_{INP} from precipitation samples. Interestingly, the feedlot IN spectra and most of our precipitation samples shown in Fig. 4 were greater than the previously derived precipitation IN upper limit, implying abundant IN active feedlot dusts, which might be involved in the precipitation formation and thereby our samples. It is noteworthy that adjacent feedlots (> 45,000 head capacity) are located within 33 miles of our sampling site. We observed approximately a two orders of magnitude increase in the upper limit of feedlot n_{INP} compared to previous precipitation study at -15°C. For $T \geq$ -15°C, there was at least one sample from each precipitation category falling in the IN spectra region of feedlot dust. Some of the hail/thunderstorm type samples had n_{INP} values in the range of feedlot samples even for the entire T range of 0°C to -25°C (Fig. 4b). For example, at -5°C, n_{INP} from our precipitation samples were in the range of 0.01 – 0.11 L^{-1} of air in the atmosphere. These findings suggest the influence of local feedlot dust on precipitations and on increase of n_{INP} upper limit for precipitation samples. Furthermore, for 0°C ≤ T ≤ -25°C, we found no precipitation sample with n_{INP} values below the lower limit from the Petters and Wright (2015) study.

Compared to all other precipitation types, hail/thunderstorm type had the highest average n_{INP} ± standard error of 0.1 ± 0.01 and 118 ± 68.1 L^{-1} at -5°C and -25°C. In addition, the snow type had the highest average n_{INP} of 0.4 ± 0.3, 0.8 ± 0.5, and 5.7 ± 2.5 L^{-1} at -10°C, -15°C, and -20°C (SI Table S3-1). The lowest n_{INP} values were observed in both the long-lasted and weak rain samples at most of the temperatures. Interestingly, we observed an order of magnitude increase in the maximum n_{INP} calculated at -5°C and -25°C in hail/thunderstorm type compared to long-lasted and weak rains. Such high values of n_{INP} in snow and hail/thunderstorm samples suggested that the INPs impact the severity of a precipitation at least in the West Texas region. These feedlot dusts could reach cloud height and be involve in local aerosol-cloud-precipitation interactions, influencing the local hydrological cycle. Further discussion regarding the feedlot contribution in INPs in our precipitation samples are provided in Section 3.4. We observed a reduced uncertainty in n_{INP} from precipitation samples at T > -10°C. For example, a two order magnitude difference was estimated at -8°C in this study, which is lower than previously reported n_{INP} uncertainty at the same temperature (Petters and Wright, 2015). Nonetheless, the discrepancy in n_{INP} still remains at high Ts. Furthermore, the lower n_{INP} values from this study were greater than the lower limit presented in Petters and Wright (2015). The upper and lower n_{INP} limit derived from this precipitation study could help in comparison studies of n_{INP} at the cloud level to the observed ice-crystal concentrations. Overall, our findings imply that the local feedlot dust contribute to the regional INPs, with an increase in the high T n_{INP} in our precipitation samples.

3.3.2. Seasonal variability and INP-precipitation relationship

The time series of cumulative n_{INP} from precipitation samples at different Ts (i.e., -5°C, -10°C, -15°C, -20°C, and -25°C) is shown in Fig. 5. The overall average, cumulative n_{INP} ± standard error is also presented in Fig. 5. For example, we observed an average n_{INP} of 0.17 ± 0.04 L^{-1} at high T such as -10°C. Figure 5b shows n_{INP} for two precipitation samples (ID# 26 and 27) observed on the same day of 12 March 2019. In total, 24 precipitation samples were collected in the year 2018 and 18 in 2019. A clear variation in high T n_{INP} at -5°C was observed with seasons due to variation in the occurrence of severe precipitations which is discussed below. Furthermore, an increase in n_{INP} at -25°C was observed in the summer of both 2018 and 2019 (Fig. 5a). Overall, 2018 had recorded the highest maximum n_{INP} at -5°C and -10°C (0.11 and 1.62 L^{-1}) compared to 2019 (0.06 and 0.65 L^{-1}). This high INPs in the year 2018 than in 2019 might be due the presence of more snow and hail/thunderstorms in the year 2018 compared to 2019. A combined total of 14 snow and hail/thunderstorm samples were collected in 2018 and a total of 10 in the year 2019. In order to elucidate this seasonal variation, we further subcategorized our sampling period into four different periods; i.e., May-August (May-Aug; which is a summer season at Canyon, TX), September-October (Sep-Oct), November-January (Nov-Jan; which is a winter season at Canyon, TX), and February-April (Feb-Apr), shown in Fig. 6a. Most of the high T (-5°C) n_{INP} were observed during May – Aug, while there was a decrease in the following seasons, with no INPs at -5°C in the Feb – Apr period. The May - Aug season was dominated by hail/thunderstorms, whereas Feb – Apr had seen mostly long-lasted and weak rains. Likewise, significantly (p-value = 0.09; student's independent t-test) higher INPs were measured at -10°C during Nov – Jan than in Feb – Apr. These findings suggested a strong seasonal variation in INPs, specifically in the high T (≥ -15°C) INPs in Canyon, TX.

The variation of INPs among the precipitation types is shown in Fig. 6b. A statistically significant (p-value ≤ 0.01; student's independent t-test) increase in high T (-5°C) n_{INP} was found in hail/thunderstorm samples compared to long-lasted rains. Additionally, we observed only one sample from weak rain type with n_{INP} at -5°C, supporting the decrease of high T INPs in the less severe precipitation types. Similarly, the distribution of n_{INP} at -25°C for weak rain type was shifted towards relatively lower values than compared with more severe precipitation types, such as hail/thunderstorm. For example, at -25°C, hail/thunderstorm type had a median n_{INP} of 22.44 L^{-1}, which was greater than what was measured in weak rain (6.19 L^{-1}) type. These results of increase in severity of precipitation with an increase in INPs were further corroborated by our findings from maximum intensity range based n_{INP} analysis (shown in Fig. 6c). For this intensity - n_{INP} analysis, we grouped all our precipitation samples into three different categories based on the observed maximum intensity (mm hr^{-1}) in each precipitation event. A significant (p-value ≤ 0.01) increase in INPs at -5°C was found when the maximum intensity was > 50 mm hr^{-1} compared to the range of 10 – 50 mm hr^{-1}. The samples from this high intensity range (> 50 mm hr^{-1}) were mostly coincided with the hail/thunderstorm precipitation types, supporting our previous findings of increase in severity of precipitation with INPs. It is also important to note that there was only one hail/thunderstorm sample which fell in the low intensity range (< 10 mm hr^{-1}). Overall, we found a strong seasonal variation in INPs, especially in the high T (-5°C and -10°C) INPs from our yearlong precipitation study. Moreover, we observed an increase in the severity of precipitation with INPs, which highlights the

Atmospheric
Chemistry
and Physics
Discussions

importance of INPs in the development and growth of severe precipitation systems in the West Texas region.

3.4. Microbiome of Feedlot and Precipitation Samples

450 We successfully generated data on the bacterial microbiome of our precipitation and feedlot dust samples. Unfortunately, our attempt to extract fungal microbe was not successful due to the limitation in sample amount. Thus, we focus on bacterial discussions hereafter. In most cases, bacterial phyla were classified to the level of genus. The majority of bacteria in all samples belonged to phyla *Proteobacteria* and *Bacteroidetes* (Fig. 7a and Table S4-1). In hailstorm samples, the main taxa of *Proteobacteria* were *Massilia* (a genus found in clinical samples, mammals, but also soil, rhizosphere and even aerosols), genera belonging to

455 the order *Sphingomonadales* (bacteria with wide metabolic abilities), *Caulobacterales* (bacteria living in diverse terrestrial and aquatic habitats, some are minor human pathogens), and *Rhizobiales* (nitrogen-fixing bacteria forming symbioses with the roots of legumes). Among the *Bacteroidetes* phylum, the genus *Marinoscillum* was relatively the most abundant. This genus is a recently described marine bacterium and it is interesting that it was found in hailstorm samples at percentages from 17.3% to 3.2% of the microbiome. Our results perhaps

460 indicate some connection with storms or winds originating from the North Atlantic Ocean (back-trajectories analyses done, but not shown). Other *Bacteroidetes* taxa with notable presence in hailstorm microbiome included *Saprospirales* and *Chitinophagales* orders with bacteria living on animals and in the gut of animals as expected.

The microbiome of one long-lasted rain sample shared members also found in hailstorms: the genus

465 *Massilia* in significant numbers (11.3% of the microbiome), bacteria of the Proteobacterial orders *Rhizobiales*, *Sphingomonadales* and *Burkholderiales*; a significant percentage (8.5%) of the marine genus *Marinoscillum* and bacteria in order *Sarospirales* of phylum *Bacteroidetes*. Our results suggest that no known ice nucleation active species detected in precipitation microbiomes. The order *Pseudomonadales*, which includes most known ice nucleation active species, was found at the limit of detection.

470

Massilia was also relatively dominant in all four feedlot samples with percentages from 6.5% to 65.4% of the microbiome. *Marinoscillum* was also found in feedlot samples from 3% to 8.5% of the microbiome, perhaps indicating some connection of these genera either with the formation of precipitation or with their presence in aerosols during precipitation events. It is noteworthy to mention that neither of these two genera

475 (*Massilia* and *Marinoscillum*) was detected in the background deposition blank sample and it is not known whether they have any ice nucleation activity. Other bacterial taxa with significant presence in feedlot samples included members of orders *Caulobacterales* and *Burkholderiales*.

Alpha diversity analysis (Shannon's Faith PD index of diversity) indicated that feedlot and hailstorm

480 samples had a lower bacterial diversity than the long-lasting rain sample (Fig. 7b). We sought to identify a possible connection between the feedlot microbiome and the microbiome of hail and rain. Beta diversity analysis compared the microbiome diversity distance of feedlot samples between themselves, as well as the microbiome diversity distance of the background deposition, hailstorm and long-lasted rain samples to feedlot samples (Fig. 7c). In all comparisons, the distance was at least 0.70, a high value not indicating a "cause and effect" connection

Atmospheric
Chemistry
and Physics
Discussions

485 between the feedlot and precipitation microbiomes. However, our detailed phylogenetic analysis showed evidence of such a connection by identifying common bacterial taxa in feedlot and precipitation microbiomes. Their absence from the background deposition blank sample may indicate local aerosol-cloud interactions leading to precipitation events, but it is not known if this is a result of any bacterial traits such as ice nucleation activity.

490

4. Conclusion

We have successfully estimated n_{INP} (per liter of air) in the immersion freezing mode from different precipitation samples collected in Canyon, TX, USA. IN spectra were derived for MPC T range (0°C to -25°C) from
495 four different precipitation types (snows, thunder/hail storms, long-lasted rains, and weak rains) using a cold-stage instrument (WT-CRAFT). Our disdrometer measurements showed a clear variation in the precipitation properties among the four different categories of precipitation samples. Severe precipitations, such as hail/thunderstorms, had the highest rainfall intensity (mm hr^{-1}) and the number of precipitation particles were highest in the snow samples. We also found an increased number of large hydrometeors (> 8.5 mm in diameter)
500 in both the snow and hail/thunderstorm samples. In contrast, there were no precipitation particles > 6.5 mm in diameter observed in the weak rain samples. Our PM concentration measurements showed no strong correlation with the measured INPs from precipitation samples. The IN spectra from each precipitation category in this study were compared with the nucleus spectra from previous precipitation based INP study (Petters and Wright, 2015). Previously derived IN spectra from local feedlot dust samples (Whiteside et al., 2018) was also used for comparing
505 n_{INP} from precipitation samples. We have found that n_{INP} values from our precipitation samples were greater than previously derived IN upper limits from precipitations. Especially, the high T ($\geq$ -15°C) INPs in some of our precipitation samples were in the same order of magnitude as of local feedlot dust samples. These findings suggested the importance of local feedlot dusts as INP sources. Moreover, we have observed a strong seasonal variation in n_{INP} in this precipitation based INP study. The May – Aug period had seen the most INPs at -5°C, while
510 none during Feb – Apr season. It is important to note that, hail/thunderstorms were predominantly observed in the May – Aug season. A statistically significant increase in high T (-5°C) INPs was observed in hail/thunderstorms compared to long-lasted rains. Except in one case, we observed no weak rain samples with INPs at -5°C. These findings suggested an increase in high T (-5°C and -10°C) INPs in severe precipitation systems like hail/thunderstorm and snow in the West Texas region. These results were further supported by our findings of
515 increased high T INPs when the rainfall intensity was > 50 mm hr^{-1}. Overall, our results showed that the INPs impact the severity of precipitation systems observed in Texas Panhandle, which represents the importance of more precipitation based INP studies in the future. We also identified the similarity in bacterial microbiome between our hailstorm and local feedlot dust samples, nevertheless, it is not known whether these microbiomes are IN active. Regardless, we did not find the previously known bacterial INPs, such as *Pseudomonas* and
520 *Xanthomonas* (Morris et al., 2004) in both the precipitation and feedlot samples. Our preliminary analysis showed that organic component was predominant in our precipitation residuals (>70%, not shown in this study), which is similar to the composition of local animal feeding dust (Hiranuma et al., 2011). This similarity might explain the observed increase in n_{INP} from precipitation samples at high Ts ($\geq$ -15°C). Therefore, it is worthwhile to characterize the local feedlot dust, as they can be the sources of INPs and can impact the local hydrological cycle.
525

Atmospheric
Chemistry
and Physics
Discussions

Open Access

The relationship between pollen and the PM concentrations has not been analyzed in this study. Collecting long-term observational pollen and other biogenic aerosol particles data for multiple years may add important knowledge regarding the role of local bioaerosols on the precipitation INPs. As for more future studies, INPs derived from precipitation samples collected over multiple years would give comprehensive

530   insight into their impact on local precipitation systems. This work highlights this need for more precipitation based INP studies from different geographical locations. Precipitation category based n_{INP} parametrizations can be applicable to any future studies as demonstrated in this study. The reduced uncertainties in n_{INP} along with the observed increase in the lower n_{INP} values from this study could help in addressing the long debated issue of INP rarity at Ts ≥ -10°C. In other words, the increased n_{INP} at high Ts from this study might minimize the

535   discrepancies between the measured INPs in the atmosphere and observed ice crystal concentrations. Accordingly, these parametrizations can help in minimizing the uncertainty in the ice-cloud formation.

Author Contributions

540

Research design: NH, JW; Measurements: HSKV, CAR, GDM, DH, JW, NH; Analysis: HSKV, DGG, NH; Writing: HSKV, NH, DGG. GDM conducted the metagenomics investigation without knowing the identity of samples.

Competing Interests

545

The authors declare that they have no conflict of interest.

Data Availability

Original data created for the study will be available in a persistent repository upon publication within www.wtamu.edu.

550   ## Acknowledgements

555   ## References

Ansmann, A., Tesche, M., Althausen, D., Müller, D., Seifert, P., Freudenthaler, V., Heese, B., Wiegner, M., Pisani, G., Knippertz, P., and Dubovik, O.: Influence of Saharan dust on cloud glaciation in southern Morocco during the Saharan Mineral Dust Experiment, J. Geophys. Res., 113, D04210, 2008.

560

Ansmann, A., Tesche, M., Seifert, P., Althausen, D., Engelmann, R., Fruntke, J., Wandinger, U., Mattis, I., and Müller, D.: Evolution of the ice phase in tropical altocumulus: SAMUM lidar observations over Cape Verde, J. Geophys. Res., 114, D17208, 2009.

565   Beall, C. M., Lucero, D., Hill, T. C., DeMott, P. J., Stokes, M. D., and Prather, K. A.: Best practices for precipitation sample storage for offline studies of ice nucleation, Atmos. Meas. Tech. Discuss., in review, 2020.

Belosi, F., and Santachiara, G.: Laboratory investigation of aerosol coating and capillarity effects on particle ice nucleation in deposition and condensation modes, Atmospheric Research, 230, 104633, 2019.
570
Chen, Q., Yin, Y., Jiang, H., Chu, Z., Xue, L., Shi, R., Zhang, X., and Chen, J.: The Roles of Mineral Dust as Cloud Condensation Nuclei and Ice Nuclei During the Evolution of a Hail Storm, Journal of Geophysical Research: Atmospheres, 124, 14262-14284, 2019.

575   Cory, K. M.: Immersion freezing of non-proteinaceous biological aerosol proxies and arctic ambient particles, M.S. thesis, West Texas A&M University, Canyon, TX, USA, 2019a.

Cory, K., Mills, J., Tobo, Y., Murata, K., Goto-Azuma, K., Whiteside, C., McCauley, B., Bouma, C., and Hiranuma, N.: Laboratory measurements of immersion freezing abilities of non-proteinaceous and proteinaceous biological particulate
580   proxies, Earth and Space Science Open Archive, 1, 2019b.

Creamean, J. M., Mignani, C., Bukowiecki, N., and Conen, F.: Using freezing spectra characteristics to identify ice-nucleating particle populations during the winter in the Alps, Atmos. Chem. Phys., 19, 8123-8140, 2019.

585   Cui, Z., Carslaw, K. S., Yin, Y., and Davies, S.: A numerical study of aerosol effects on the dynamics and microphysics of a deep convective cloud in a continental environment, J. Geophys. Res., 111, D05201, 2006.

David, R. O., Marcolli, C., Fahrni, J., Qiu, Y., Sirkin, Y. A. P., Molinero, V., Mahrt, F., Brühwiler, D., Lohmann, U., and Kanji, Z. A.: Pore condensation and freezing is responsible for ice formation below water saturation for porous particles,
590   Proceedings of the National Academy of Sciences, 116, 8184-8189, 2019.

de Boer, G., Hashino, T., and Tripoli, G. J.: Ice nucleation through immersion freezing in mixed-phase stratiform clouds: Theory and numerical simulations, Atmospheric Research, 96, 315-324, 2010.

595   de Boer, G., Morrison, H., Shupe, M., and Hildner, R.: Evidence of liquid dependent ice nucleation in high-latitude stratiform clouds from surface remote sensors, Geophysical Research Letters, 38, L01803, 2011.

DeMott, P. J., Prenni, A. J., Liu, X., Kreidenweis, S. M., Petters, M. D., Twohy, C. H., Richardson, M. S., Eidhammer, T., and Rogers, D. C.: Predicting global atmospheric ice nuclei distributions and their impacts on climate,
600   Proceedings of the National Academy of Sciences, 107, 11217-11222, 2010.

DeMott, P. J., Hill, T. C. J., Petters, M. D., Bertram, A. K., Tobo, Y., Mason, R. H., Suski, K. J., McCluskey, C. S., Levin, E. J. T., Schill, G. P., Boose, Y., Rauker, A. M., Miller, A. J., Zaragoza, J., Rocci, K., Rothfuss, N. E., Taylor, H. P., Hader, J. D., Chou, C., Huffman, J. A., Pöschl, U., Prenni, A. J., and Kreidenweis, S. M.: Comparative measurements
605   of ambient atmospheric concentrations of ice nucleating particles using multiple immersion freezing methods and a continuous flow diffusion chamber, Atmos. Chem. Phys., 17, 11227-11245, 2017.

Després, V., Huffman, J. A., Burrows, S. M., Hoose, C., Safatov, A., Buryak, G., Fröhlich-Nowoisky, J., Elbert, W., Andreae, M., Pöschl, U., and Jaenicke, R.: Primary biological aerosol particles in the atmosphere: a review, Tellus B: Chemical and
610   Physical Meteorology, 64, 15598, 2012.

Durant, A. J., and Shaw, R. A.: Evaporation freezing by contact nucleation inside-out, Geophysical Research Letters, 32, L20814, 2005.

615   Ervens, B., and Feingold, G.: Sensitivities of immersion freezing: Reconciling classical nucleation theory and deterministic expressions, Geophysical Research Letters, 40, 3320-3324, 2013.

Fan, J., Leung, L. R., Rosenfeld, D., and DeMott, P. J.: Effects of cloud condensation nuclei and ice nucleating particles on precipitation processes and supercooled liquid in mixed-phase orographic clouds, Atmos. Chem.
620   Phys., 17, 1017–1035, 2017.

Field, P. R., Heymsfield, A. J., Shipway, B. J., DeMott, P. J., Pratt, K. A., Rogers, D. C., Stith, J., and Prather, K. A.: Ice in clouds experiment–layer clouds. Part II: Testing characteristics of heterogeneous ice formation in lee wave clouds, Journal of the atmospheric sciences, 69, 1066-1079, 2012.
625
Hande, L. B., and Hoose, C.: Partitioning the primary ice formation modes in large eddy simulations of mixed-phase clouds, Atmos. Chem. Phys., 17, 14105-14118, 2017.

Hartmann, D. L., Ockert-Bell, M. E., and Michelsen, M. L.: The effect of cloud type on Earth's energy balance: Global
630   analysis, Journal of Climate, 5, 1281-1304, 1992.

Hiranuma, N., Brooks, S. D., Gramann, J., and Auvermann, B. W.: High concentrations of coarse particles emitted from a cattle feeding operation, Atmos. Chem. Phys., 11, 8809–8823, 2011.

635   Hiranuma, N., Augustin-Bauditz, S., Bingemer, H., Budke, C., Curtius, J., Danielczok, A., Diehl, K., Dreischmeier, K., Ebert, M., Frank, F., Hoffmann, N., Kandler, K., Kiselev, A., Koop, T., Leisner, T., Möhler, O., Nillius, B., Peckhaus, A., Rose, D., Weinbruch, S., Wex, H., Boose, Y., DeMott, P. J., Hader, J. D., Hill, T. C. J., Kanji, Z. A., Kulkarni, G., Levin, E. J. T., McCluskey, C. S., Murakami, M., Murray, B. J., Niedermeier, D., Petters, M. D., O'Sullivan, D., Saito, A., Schill, G. P., Tajiri, T., Tolbert, M. A., Welti, A., Whale, T. F., Wright, T. P., and Yamashita, K.: A comprehensive
640   laboratory study on the immersion freezing behavior of illite NX particles: a comparison of 17 ice nucleation measurement techniques, Atmos. Chem. Phys., 15, 2489–2518, 2015.

Hiranuma, N., Adachi, K., Bell, D. M., Belosi, F., Beydoun, H., Bhaduri, B., Bingemer, H., Budke, C., Clemen, H.-C., Conen, F., Cory, K. M., Curtius, J., DeMott, P. J., Eppers, O., Grawe, S., Hartmann, S., Hoffmann, N., Höhler, K.,
645   Jantsch, E., Kiselev, A., Koop, T., Kulkarni, G., Mayer, A., Murakami, M., Murray, B. J., Nicosia, A., Petters, M. D., Piazza, M., Polen, M., Reicher, N., Rudich, Y., Saito, A., Santachiara, G., Schiebel, T., Schill, G. P., Schneider, J., Segev, L., Stopelli, E., Sullivan, R. C., Suski, K., Szakáll, M., Tajiri, T., Taylor, H., Tobo, Y., Ullrich, R., Weber, D., Wex, H., Whale, T. F., Whiteside, C. L., Yamashita, K., Zelenyuk, A., and Möhler, O.: A comprehensive characterization of ice nucleation by three different types of cellulose particles immersed in water, Atmos. Chem. Phys., 19, 4823–
650   4849, 2019.

Kanji, Z. A., and Abbatt, J. P. D.: Laboratory studies of ice formation via deposition mode nucleation onto mineral dust and n-hexane soot samples, Journal of Geophyical Research, 111, D16204, 2006.

655   Kanji, Z. A., Ladino, L. A., Wex, H., Boose, Y., Burkert-Kohn, M., Cziczo, D. J., and Krämer, M.: Overview of ice nucleating particles, Meteorological Monographs, 58, 1.1-1.33, 2017.

Koop, T., Luo, B., Tsias, A., and Peter, T.: Water activity as the determinant for homogeneous ice nucleation in aqueous solutions, Nature, 406, 611-614, 2000.
660
Levin, E. J., DeMott, P. J., Suski, K. J., Boose, Y., Hill, T. C. J., McCluskey, C. S., Schill, G. P., Rocci, K., Al-Mashat, H., Kristensen, L. J., Cornwell, G., Prather, K., Tomlinson, J., Mei, F., Hubbe, J., Pekour, M., Sullivan, R., Leung, L. R., and Kreidenweis, S. M.: Characteristics of ice nucleating particles in and around California winter storms, Journal of Geophysical Research: Atmospheres, 124, 11530-11551, 2019.
665
Lohmann, U., and Feichter, J.: Global indirect aerosol effects: a review, Atmos. Chem. Phys., 5, 715-737, 2005.

Lohmann, U., Stier, P., Hoose, C., Ferrachat, S., Kloster, S., Roeckner, E., and Zhang, J.: Cloud microphysics and aerosol indirect effects in the global climate model ECHAM5-HAM, Atmos. Chem. Phys., 7, 3425-3446, 2007.
670
Marcolli, C.: Deposition nucleation viewed as homogeneous or immersion freezing in pores and cavities, Atmos. Chem. Phys., 14, 2071-2104, 2014.

McMurdie, P. J., and Holmes, S.: phyloseq: an R package for reproducible interactive analysis and graphics of microbiome
675   census data, PloS one, 8, e61217, 2013.

Möhler, O., Benz, S., Saathoff, H., Schnaiter, M., Wagner, R., Schneider, J., Walter, S., Ebert, V., and Wagner, S.: The effect of organic coating on the heterogeneous ice nucleation efficiency of mineral dust aerosols, Environmental Research Letters, 3, 025007, 2008.
680
Morris, C. E., Georgakopoulos, D. G., and Sands, D. C.: Ice nucleation active bacteria and their potential role in precipitation, J. Phys. IV France, 121, 87-103, 2004.

Mülmenstädt, J., Sourdeval, O., Delanoë, J., and Quaas, J.: Frequency of occurrence of rain from liquid-, mixed-,
685 and ice-phase clouds derived from A-Train satellite retrievals, Geophysical Research Letters, 42, 6502-6509, 2015.

Murray, B. J., O'sullivan, D., Atkinson, J. D., and Webb, M. E.: Ice nucleation by particles immersed in supercooled cloud
droplets, Chem. Soc. Rev., 41, 6519-6554, 2012.

690 Niedermeier, D., Shaw, R. A., Hartmann, S., Wex, H., Clauss, T., Voigtländer, J., and Stratmann, F.: Heterogeneous ice
nucleation: exploring the transition from stochastic to singular freezing behavior, Atmos. Chem. Phys., 11, 8767-8775,
2011.

Petters, M. D., and Wright, T. P.: Revisiting ice nucleation from precipitation samples, Geophysical Research Letters, 42,
695 8758-8766, 2015.

Phillips, V. T. J., Donner, L. J., and Garner, S. T.: Nucleation processes in deep convection simulated by a cloud-system-
resolving model with double-moment bulk microphysics, Journal of the atmospheric sciences, 64, 738-761, 2007.

700 Rodriguez, C. A., Vepuri, H. S., and Hiranuma, N.: Implications of Precipitation Particle Properties for Improved
Understanding of Ice-Nucleating Particles in West Texas, Earth and Space Science Open Archive, 1, 2020.

Rosenfeld, D., Lohmann, U., Raga, G. B., O'Dowd, C. D., Kulmala, M., Fuzzi, S., Reissell, A., and Andreae, M. O.: Flood or
drought: How do aerosols affect precipitation?, Science, 321, 1309-1313, 2008.
705
Satheesh, S. K., and Moorthy, K. K.: Radiative effects of natural aerosols: A review, Atmospheric Environment, 39, 2089-
2110, 2005.

Schiebel, T.: Ice nucleation activity of soil dust aerosols, Ph.D. thesis, Institute of Meteorology and Climate Research,
710 Karlsruhe Institute of Technology, Germany, 2017.

Stopelli, E., Conen, F., Morris, C. E., Herrmann, E., Bukowiecki, N., and Alewell, C.: Ice nucleation active particles are
efficiently removed by precipitating clouds, Scientific Reports, 5, 16433, 2015.

715 Tokay, A., Wolff, D. B., and Petersen, W. A.: Evaluation of the new version of the laser-optical disdrometer, OTT Parsivel2,
Journal of Atmospheric and Oceanic Technology, 31, 1276-1288, 2014.

Vaid, B. H., and San Liang, X.: Tropospheric temperature gradient and its relation to the South and East Asian precipitation
variability, Meteorology and Atmospheric Physics, 127, 579-585, 2015.
720
Vali, G.: Quantitative evaluation of experimental results on the heterogeneous freezing nucleation of supercooled liquids,
Journal of the Atmospheric Sciences, 28, 402-409, 1971.

Vali, G., DeMott, P. J., Möhler, O., and Whale, T. F.: A proposal for ice nucleation terminology, Atmos. Chem.
725   Phys., 15, 10263-10270, 2015.

Van den Heever, S. C., Carrió, G. G., Cotton, W. R., DeMott, P. J., and Prenni, A. J.: Impacts of nucleating aerosol
on Florida storms. Part I: Mesoscale simulations, Journal of the atmospheric sciences, 63, 1752-1775, 2006.

730   Vergara-Temprado, J., Miltenberger, A. K., Furtado, K., Grosvenor, D. P., Shipway, B. J., Hill, A. A., Wilkinson, J. M., Field,
P. R., Murray, B. J., and Carslaw, K. S.: Strong control of Southern Ocean cloud reflectivity by ice-nucleating particles,
Proceedings of the National Academy of Sciences, 115, 2687-2692, 2018.

Whiteside, C., Auvermann, B. W., Bush, J., Goodwin, C., McFarlin, R., and Hiranuma, N.: Ice Nucleation Activity of Dust
735   Particles Emitted from a Cattle Feeding Operation in the Texas Panhandle, 98th American Meteorological Society Annual
Meeting, Austin, TX, USA, 8 January 2018, 250, 2018.

Yang, H., Xiao, H., and Guo, C.: Effects of Aerosols as Ice Nuclei on the Dynamics, Microphysics and Precipitation of Severe
Storm Clouds, Atmosphere, 10, 783, 2019.
740
Zhao, B., Wang, Y., Gu, Y., Liou, K.-N., Jiang, J. H., Fan, J., Liu, X., Huang, L., and Yung, Y. L.: Ice nucleation by
aerosols from anthropogenic pollution, Nature geoscience, 12, 602-607, 2019.

745   **List of Abbreviations**

C_{INP}	Nucleus concentration in Precipitation suspension
CWC	Cloud water content
DF	Dilution Fold
750 D_p	Precipitation particle diameter
$f_{unfrozen}$	Unfrozen fraction (ratio of number of unfrozen droplets to total number of droplets)
IoT	Internet of Things
IN	Ice-nucleation
755 INP	Ice-nucleating Particle
LoRaWAN	Long Range and Wide Area Network
MPC	Mixed-phase cloud
n_{INP}	INP concentration
NWS	National Weather Service

760   PM   Particulate Matter

ρ_w Unit density of water

SI   Supplemental Information

STP   Standard Temperature and Pressure

T Temperature

765   V_{air} Sample air volume at cloud level

V_d Volume of the droplet

V_l Precipitation sample volume

WT-CRAFT   West Texas Cryogenic Refrigerator Applied to Freezing Test
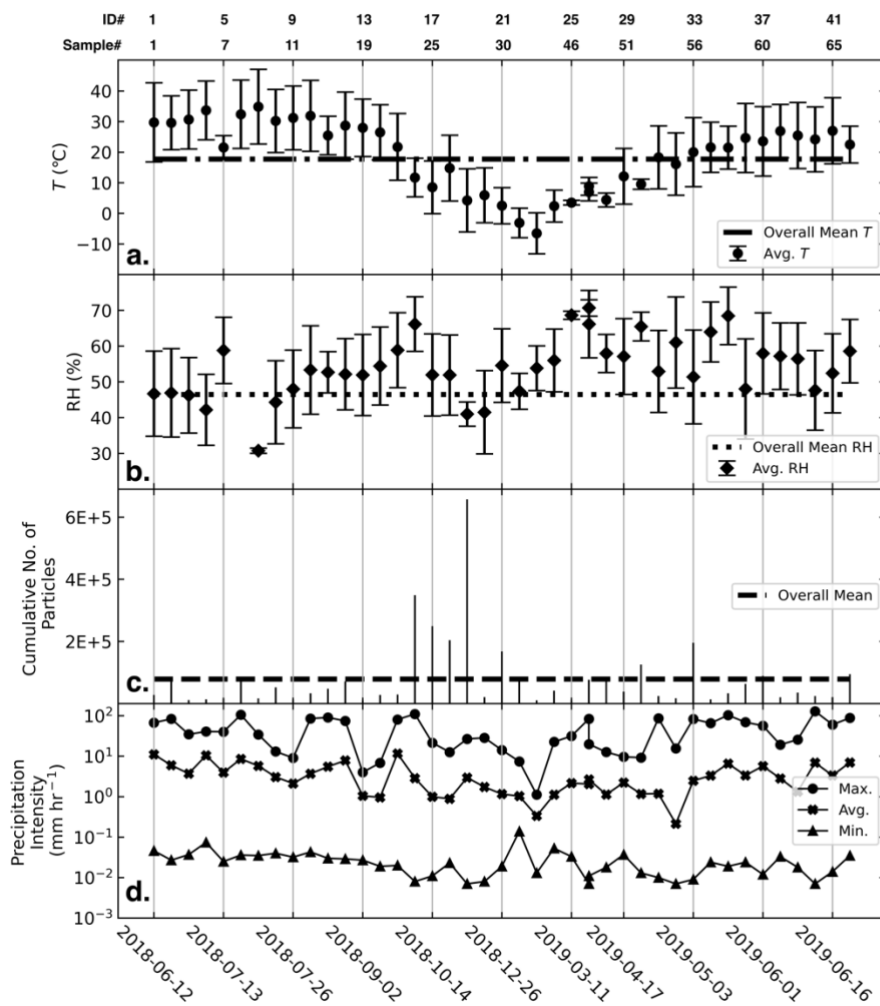
Figures

Figure 1. Time series of disdrometer and IoT sensor measurements of (a) average *T* ± standard deviation, (b) average relative humidity ± standard deviation, (c) cumulative number of detected hydrometeors in each precipitation event, and (d) maximum, average, and minimum intensity for each precipitation sample.
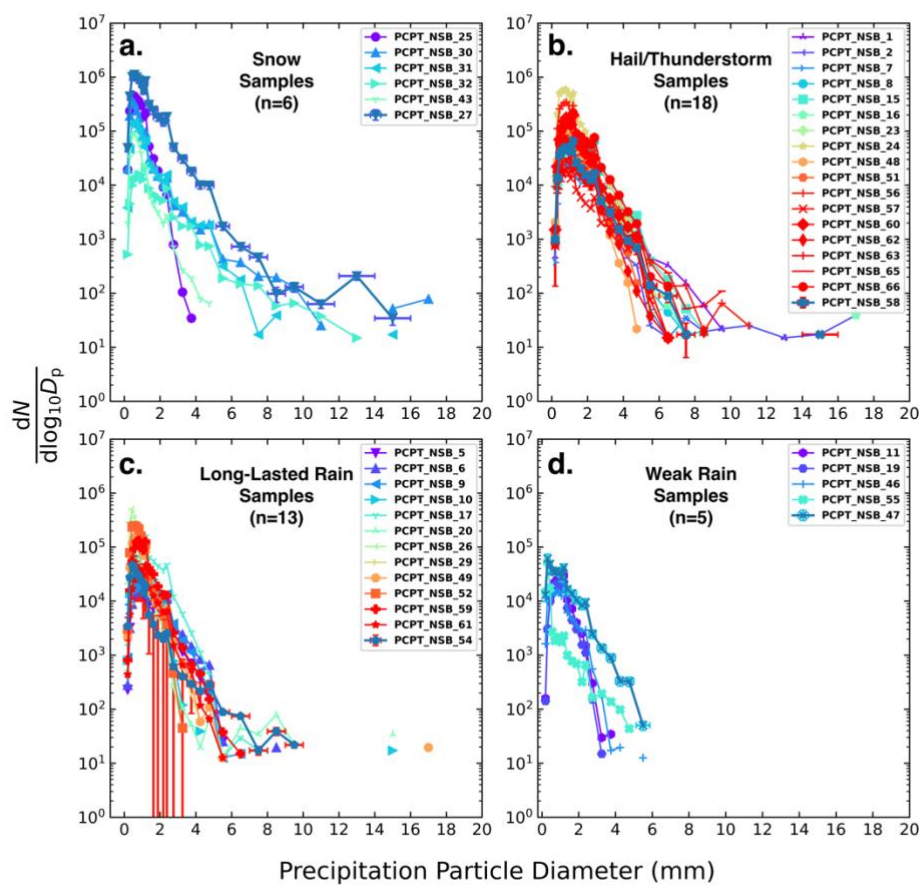
Figure 2. Size distribution of precipitation particles detected in (a) Snow, (b) Hail/Thunderstorm, (c) Long-lasted rain, and (d) Weak rain samples with varying uncertainty in diameter (mm). The X-axis error bars are ± 1.0 mm of size class for diameter < 2mm and ± 0.5 mm of size class for diameter > 2mm. The Y-axis error bars represent standard errors at each diameter. The number of precipitation samples in each category is shown by the value of 'n'.

Atmospheric
Chemistry
and Physics
Discussions

830

835

840

845

850
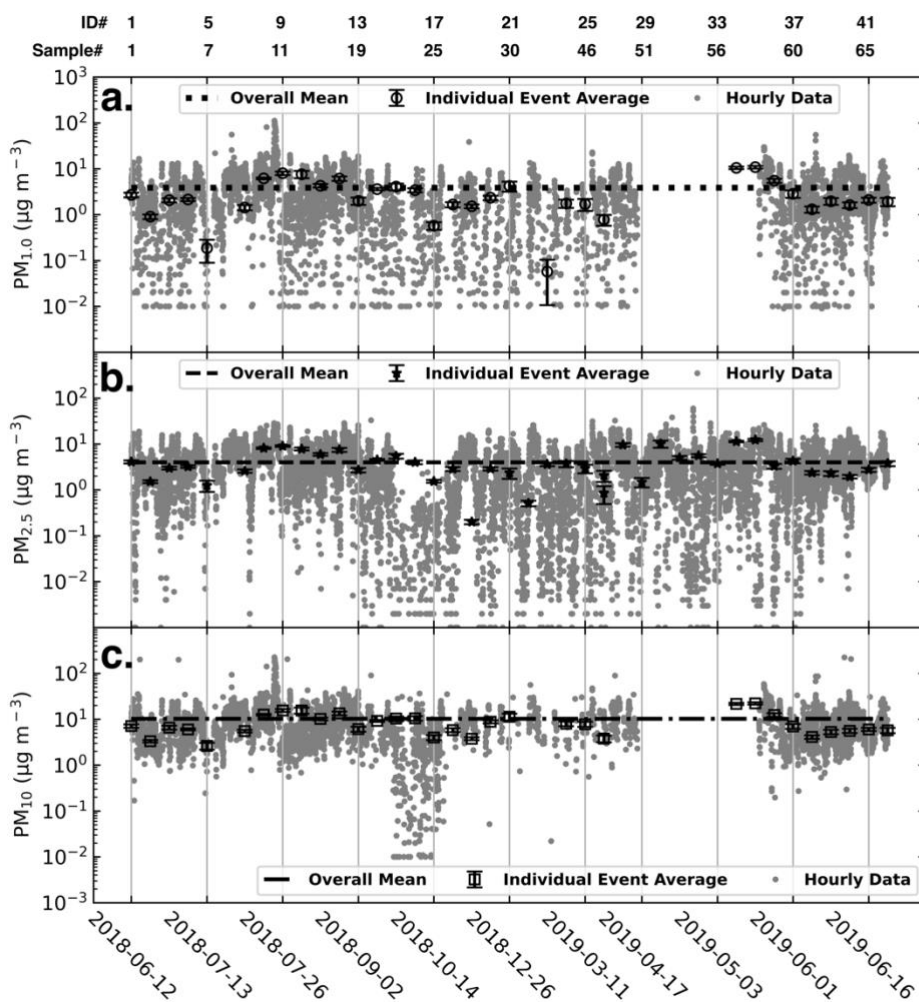
Figure 3. Time series of IoT air quality sensor measurements of (a) PM$_{1.0}$, (b) PM$_{2.5}$, and (c) PM$_{10}$ for each precipitation event. Hourly data include the non-precipitation periods (grey dots). The Y-axis error bars are standard errors measured for each precipitation event.
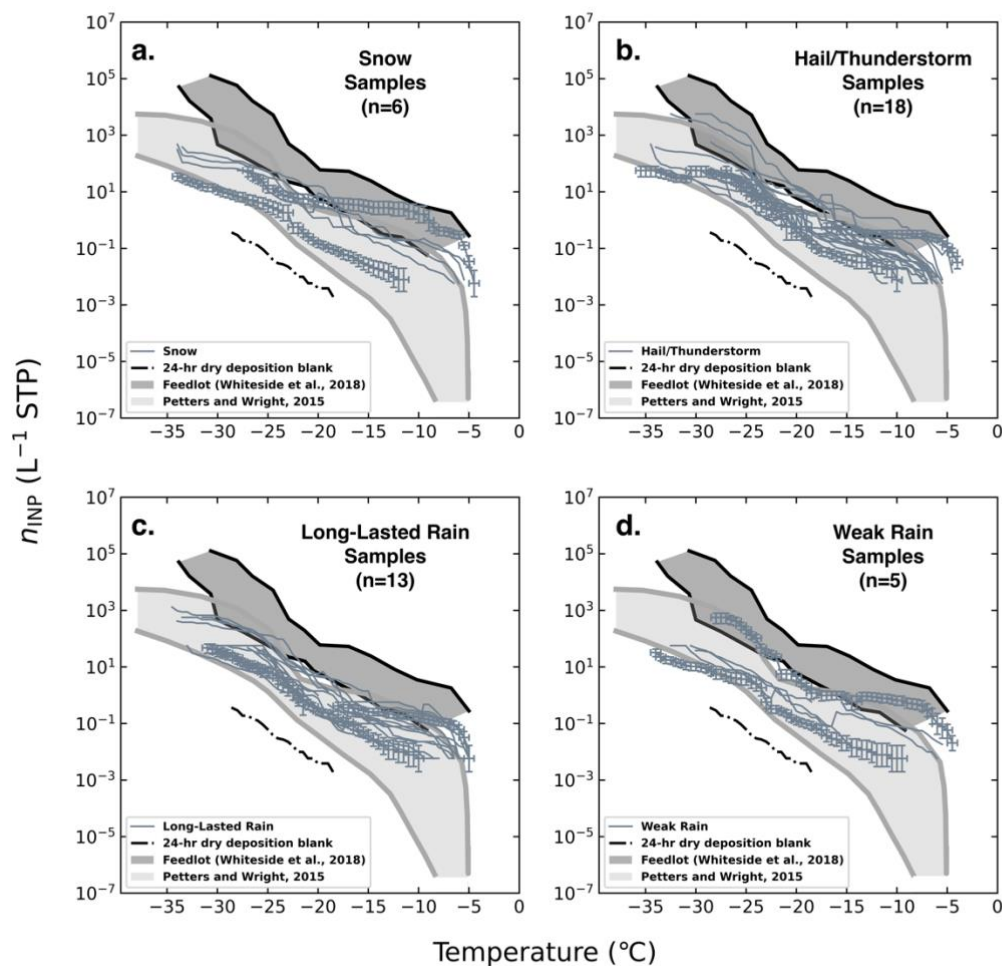
855

860

865

870

875

880

Figure 4. IN spectra of (a) Snow, (b), Hail/Thunderstorm, (c) Long-Lasted rain, and (d) Weak rain samples superposed on
885   nucleation spectra from previous studies. The X-axis error bars represent constant uncertainty of ± 0.5°C in temperature.
The Y-axis error bars are 95% confidence interval for n_{INP} shown only for two samples from each category. The number of
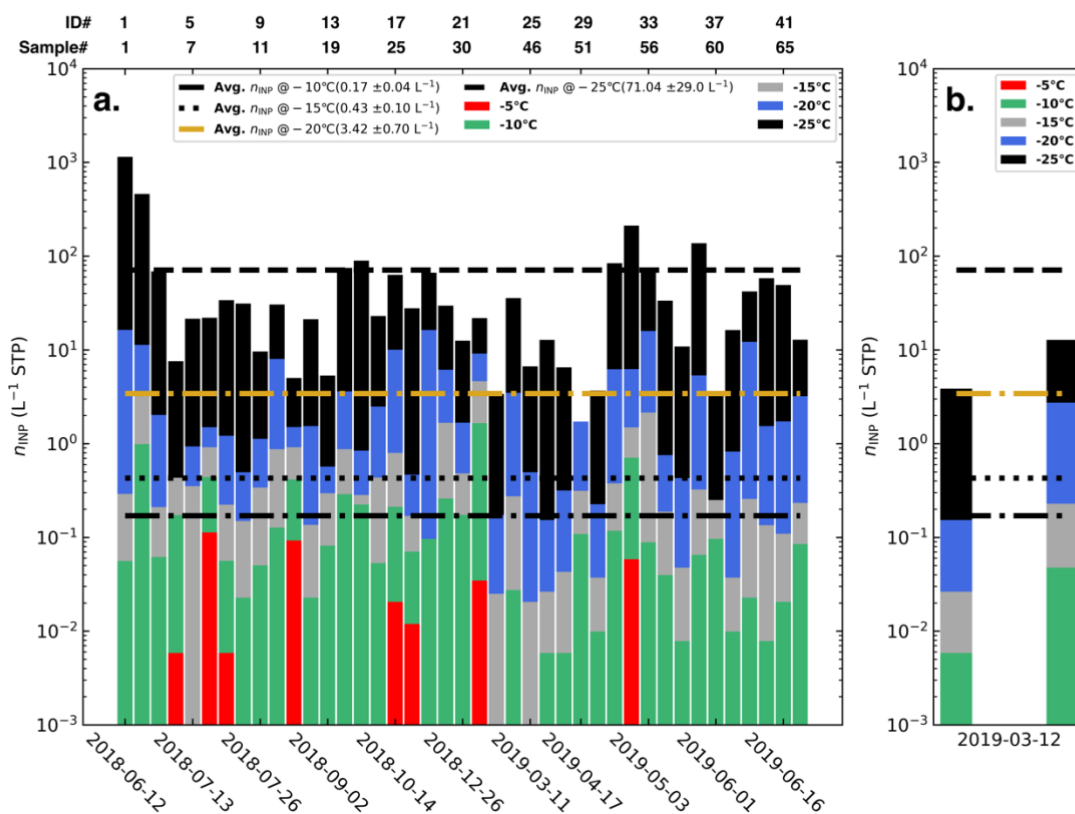precipitation samples in each category is shown by the value of 'n'.

Figure 5. (a) Time series of cumulative n_{INP} (L^{-1} air) in each precipitation sample at different temperatures. (b) n_{INP} for two precipitation samples (ID# 26 and 27) observed on the same day of 12 March 2019. The uncertainty in the average n_{INP} at each temperature (± numbers in parentheses) is the standard error calculated for 42 samples.
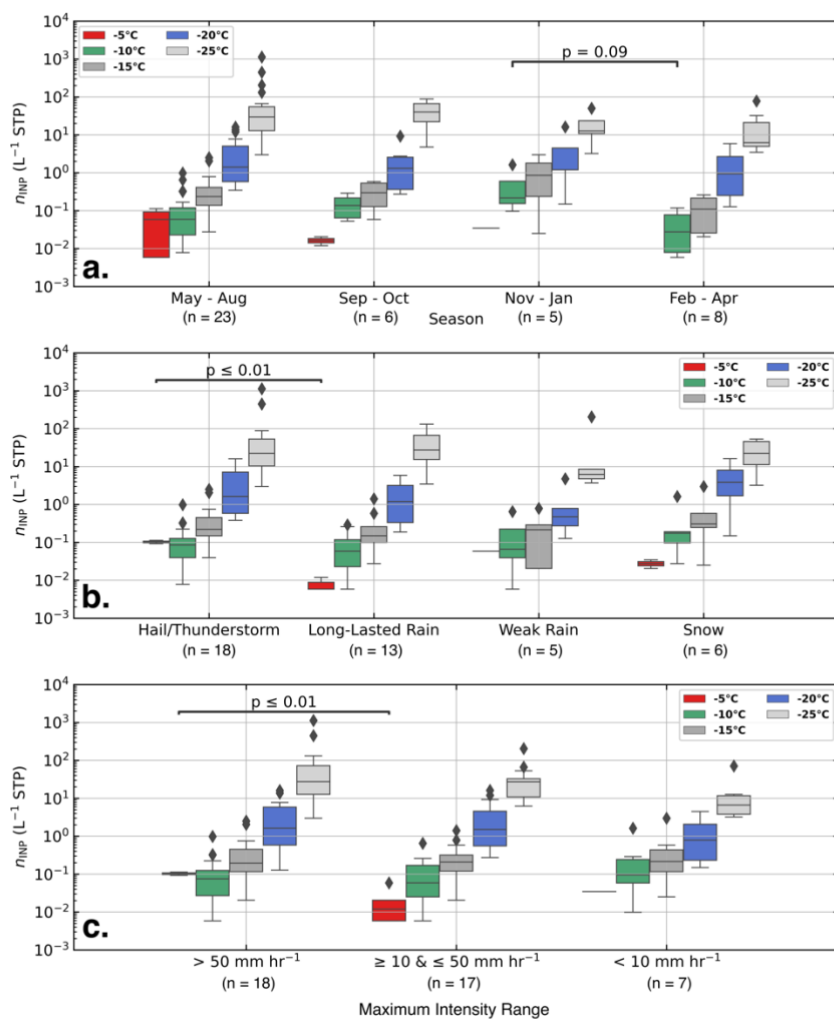
26

900

905

910

915

920

Figure 6. The distribution of n_{INP} for different (a) seasons, (b) precipitation types, and (c) range of maximum intensity observed in precipitation sample. The p-value from student's independent t-test is also shown by 'p' at different Ts between different categories. The solid line in the box is median n_{INP} and the box edges are the inter-quartile ranges q1 (25 percentile) and q3 (75 percentile). The diamond markers are the outliers with maximum n_{INP} values.
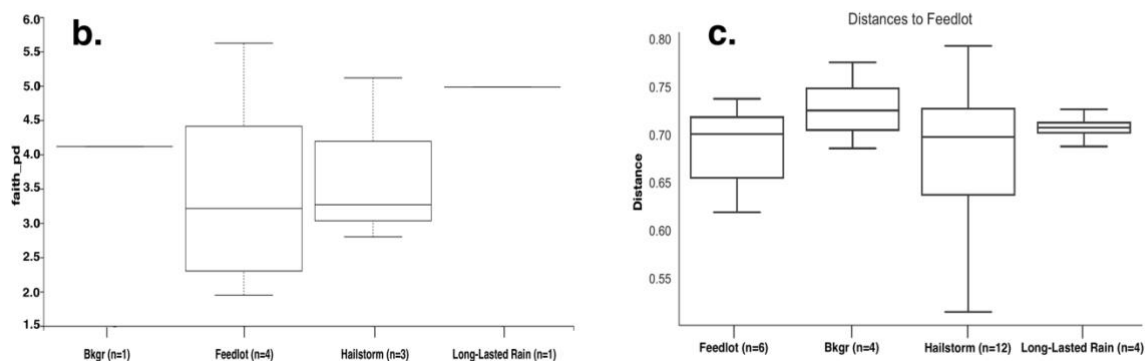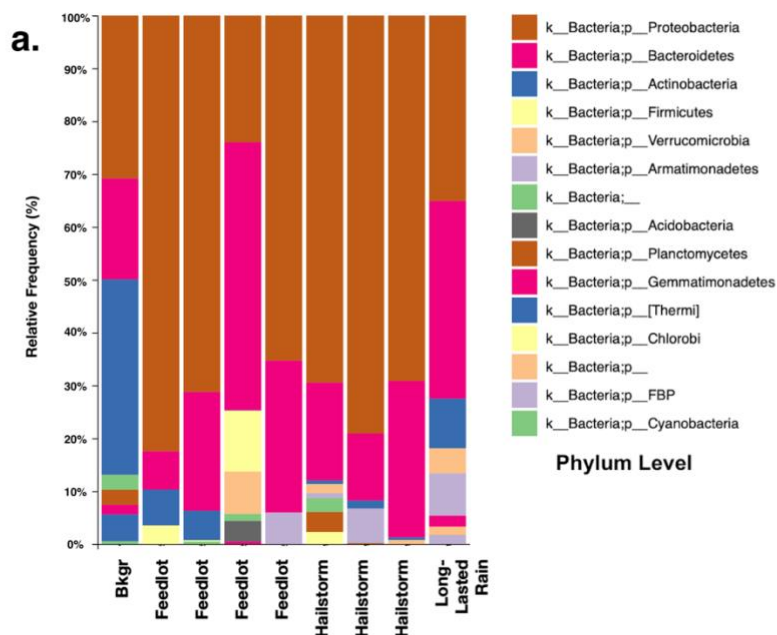
925

Figure 7. Metagenomics analysis of precipitation and feedlot dust samples showing (a) Relative Frequency (%) or abundance of Bacterial taxonomy, (b) alpha-diversity analysis with Faith's PD index of diversity (Y-axis), and (c) beta-diversity analysis comparing microbial distance of feedlot samples between themselves, as well as the microbiome diversity distance of other samples. 'Bkgr' represents the 24-hour dry deposition blank sample.